Biochimica et Biophysica Acta 1828 (2013) 2204–2214

Contents lists available at SciVerse ScienceDirect

Biochimica et Biophysica Acta

journal homepage: www.elsevier.com/locate/bbamem

Phase diagram of a 4-component lipid mixture: DSPC/DOPC/POPC/chol

Tatyana M. Konyakhina [a], Jing Wu [b], James D. Mastroianni [a], Frederick A. Heberle [c], Gerald W. Feigenson [a,*]

[a] Department of Molecular Biology and Genetics, Cornell University, Ithaca, NY 14853, USA
[b] Department of Biophysics, University of Michigan, Ann Arbor, MI 48109, USA
[c] Biology and Soft Matter Division, Oak Ridge National Laboratory, Oak Ridge, TN 37831, USA

ARTICLE INFO

Article history:
Received 29 December 2012
Received in revised form 20 May 2013
Accepted 22 May 2013
Available online 7 June 2013

Keywords:
4-Component lipid phase diagram
Quaternary phase diagram
Modulated phase
3-Dye method
Competing interaction
Lipid raft

ABSTRACT

We report the first 4-component phase diagram for the lipid bilayer mixture, DSPC/DOPC/POPC/chol (distearoylphosphatidylcholine/dioleoylphosphatidylcholine/1-palmitoyl, 2-oleoylphosphatidylcholine/cholesterol). This phase diagram, which has macroscopic Ld + Lo phase domains, clearly shows that all phase boundaries determined for the 3-component mixture containing DOPC transition smoothly into the boundaries for the 3-component mixture containing POPC, which has nanoscopic phase domains of Ld + Lo. Our studies start from two published ternary phase diagrams, and show how these can be combined into a quaternary phase diagram by study of a few hundred samples of intermediate compositions.

1. Introduction

Phase diagrams of chemically well-defined lipid mixtures help to clarify the behavior of biological membranes. In particular, mixtures of a high-melting phosphatidylcholine or sphingomyelin, a low-melting PC, and cholesterol have proven to be especially useful. These 3-component mixtures show coexisting bilayer phases over much of the composition space. A standard format for showing the phase behavior of all possible combinations of a 3-component mixture is the triangular phase diagram, or "Gibbs Triangle". The particular phase behavior where liquid-disordered (Ld) and liquid-ordered (Lo) phases coexist has been termed the "raft region", and might provide a useful model for understanding behaviors of the outer leaflet of animal cell plasma membranes.

Lipid compositional phase diagrams describe the occurrence and location in composition space of phase types (e.g., solid gel Lβ, liquid-ordered Lo, and liquid-disordered Ld) and their coexistence regions at equilibrium. For 3-component lipid mixtures, many fluorescence imaging-based studies have focused on either DOPC or else diphytanoyl-PC as the low-melting lipid, because the region of coexisting Ld + Lo phases shows easily identifiable macroscopic phase domains in giant unilamellar vesicles (GUVs), whether the high-melting lipid is a SM, DPPC, or DSPC [1–4]. In contrast, Ld + Lo phase domains are not visible with standard light microscopy when (i) the low-melting lipid component has one saturated acyl chain and one monounsaturated chain, e.g., POPC [3,5] or SOPC [5]; or (ii) the low-melting lipid is DLPC [6, M. Doktorova unpublished results]. In this case, domains can be detected by some spectroscopic methods, for example, by fluorescent or spin-label probes that partition between the domains [7,8], or by neutron scattering without probes [9]. In brief, methods sensitive to submicron length scales consistently imply liquid phase heterogeneity in POPC- and SOPC-containing ternary mixtures [7–12]. The size scale of phase domains found with POPC or SOPC is therefore below the optical diffraction limit, or "nanoscopic". Such small phase domains might be a good model for the outer leaflet of animal cell plasma membrane, which also seems to have nanoscopic coexisting Ld + Lo phase domains [13–15]: Liquid–liquid phase separation has been detected in vivo in cell membranes using techniques including FRET [16], FRAP [17], ESR [18], and super resolution optical methods [19–21].

Abbreviations: DLPC, 1,2-Dilauroyl-*sn*-glycero-3-phosphocholine; DPPC, 1,2-Dipalmitoyl-*sn*-glycero-3-phosphocholine; DSPC, 1,2-Distearoyl-*sn*-glycero-3-phosphocholine; DOPC, 1,2-Dioleoyl-*sn*-glycero-3-phosphocholine; POPC, 1-Palmitoyl-2-oleoyl-*sn*-glycero-3-phosphocholine; SOPC, 1-Stearoyl-2-oleoyl-*sn*-glycero-3-phosphocholine; PC, Phosphatidylcholine; SM, Sphingomyelin; DHE, Ergosta-5,7,9(11),22-tetraen-3β-ol; BoDIPY-PC, 2-(4,4-Difluoro-5,7-dimethyl-4-bora-3a,4a-diaza-s-indacene-3-pentanoyl)-1-hexadecanoyl-*sn*-glycero-3-phosphocholine; C12:0-DiI, 1,1′-didodecyl-3,3,3′,3′-tetramethylindocarbocyanine perchlorate; C20:0-DiI, 1,1′-dieicosanyl-3,3,3′,3′-tetramethylindocarbocyanine perchlorate; TOE, Trp-Oleoyl Ester, N-oleoyl-dl-tryptophan ethyl ester; Chol, Cholesterol; TLC, Thin-layer chromatography; GUV, Giant unilamellar vesicle; RSE, Rapid solvent exchange; FRET, Förster resonance energy transfer; SAE, Sensitized acceptor emission; RRE, Region of reduced efficiency; REE, Region of enhanced efficiency; RHS, Right hand side, refers to right side of phase diagram, i.e.,, at higher χ_{DSPC}; LHS, Left hand side refers to left side of phase diagram, i.e. at lower χ_{DSPC}; T1–T6, Trajectories 1–6. bSM, sphingomyelin derived from porcine brain

* Corresponding author. Tel.: +1 607 255 4744; fax: +1 607 255 6249.
E-mail address: gwf3@cornell.edu (G.W. Feigenson).

0005-2736/$ – see front matter © 2013 Elsevier B.V. All rights reserved.
http://dx.doi.org/10.1016/j.bbamem.2013.05.020

In cells, the range of size scales of any phase domains, as well as domain shape and connectivity, are not known. Furthermore, it is quite possible that membranes of living cells use spatial organization on multiple length scales, rather than one special size. We would benefit from chemically simple model systems that also have phase coexistence that spans the range from nanoscopic to macroscopic, thus enabling study of a range of domain sizes [22]. Here we explore the complexity of such a lipid mixture. We find that four components are the minimum to exhibit the range of size scales of coexisting phase domains from nanometers to microns as a function of mixture lipid composition. Unexpectedly, we discovered that the transition from small to large Ld + Lo domains is not at all linear, but instead passes through a compositional range in which phases show a variety of shapes and sizes [23,24]. The compositional location of this range might be significant, and by solving the entire quaternary mixture phase behavior, we are able to place this region of "modulated phases" in composition space.

A challenge for constructing a phase diagram is to determine phase boundaries with sufficient precision to establish (i) every phase region; (ii) whether any stoichiometric compositions appear; (iii) whether any phase boundaries intersect the binary axes; and (iv) comparisons of phase diagrams when, for example, lipid chain lengths differ. Such precision requires examination of a large number of samples. For example, with 20 samples binary mixtures can yield ~+/−5 mol% compositional resolution. This much uncertainty would be acceptable for certain studies, but not in cases where the uncertainty is comparable to the compositional range of interest. Ternary mixtures would require approximately 400 samples of different compositions to achieve +/−5 mol% resolution, and quaternary mixtures would require nearly 8000 samples to evenly cover the entire composition space. A second problem is that the location of phase boundaries is not always well marked by changes in fluorescence or other phase-sensitive measurements. In order to solve this problem, we introduce here a new method to locate phase boundaries with higher accuracy. Our studies, at 2 mol% compositional resolution for most boundaries, start from two published ternary phase diagrams [4,7], and show how these can be combined into a quaternary phase diagram by study of just a few hundred samples of intermediate compositions.

We note that a different view of the DSPC/POPC/chol mixture is that no Ld + Lo "nanodomain phase separation" occurs, and instead, fluctuations in the vicinity of a critical point give rise to transient changes of bilayer physical properties [25–27]. As we make clear below, the findings described here of continuous phase boundaries between DSPC/DOPC/chol and DSPC/POPC/chol over the entire composition space, support the view that Ld + Lo phase coexistence occurs whether phase domains are small or large, with all regions throughout the tetrahedron in accord with the Gibbs Phase Rule.

2. Materials and methods

2.1. Materials

Phospholipids were purchased from Avanti Polar Lipids Inc. (Alabaster, AL), and cholesterol from Nu-Chek Prep, Inc. (Elysian, MN). Fluorescent dyes C20:0-DiI, C12:0-DiI, and BoDIPY-PC were from Invitrogen Corporation (Carlsbad, CA), DHE was from Sigma-Aldrich (St. Louis, MO), and TOE (tryptophan oleoyl ester) was a gift from Erwin London. Phospholipid stocks were quantitated by phosphate assay, and purity verified to be >99% by thin-layer chromatography (TLC) of ~20 μg of lipid on washed and activated Adsorbosil TLC plates (Alltech Associates Inc., Deerfield, IL), developed in a solvent system chloroform/methanol/water (65/25/4). Cholesterol stocks were prepared analytically and purity checked with TLC in petroleum ether/diethyl ether/chloroform (7/3/3). Fluorescent dyes were checked for purity with the following solvent systems: BoDIPY-PC in chloroform/methanol/water (65/25/4); C12:0-DiI in chloroform/methanol (10/1); C20:0-DiI in petroleum ether/diethyl ether/chloroform (7/3/3); and TOE in hexane/ethyl acetate (3/1). Concentrations of fluorescent dyes were measured by absorption spectroscopy using an HP 8452A spectrophotometer (Hewlett-Packard Company, Palo Alto, CA).

2.2. Terminology

Whereas at constant temperature the ternary mixture phase behavior is conveniently represented in the plane of a Gibbs Triangle, the quaternary mixture phase behavior is best shown in the volume of a tetrahedron. Our construction of the quaternary phase diagram begins with the two ternary mixtures DSPC/DOPC/chol [4] and DSPC/POPC/chol [7] that form two triangular faces of the tetrahedron for DSPC/DOPC/POPC/chol. The tetrahedral phase diagram can be thought of as the locus of all phase observations traveling through composition space from one ternary mixture to the other, replacing POPC by DOPC. We find it convenient to refer to compositions within the tetrahedron between DOPC-containing and POPC-containing triangular faces in terms of the fractional replacement of POPC by DOPC, $\rho \equiv [DOPC] / ([DOPC] + [POPC])$. Thus, the POPC-containing face of the tetrahedron has $\rho = 0$, whereas the DOPC-containing face has $\rho = 1$.

We use the term "trajectory" to mean a series of samples along a specified path of compositions. Trajectories are used to examine the compositional dependence of a measurement such as fluorescence; in this study, trajectories were used to find the dependence of phase boundaries on ρ, that is, to connect the 3-component phase diagrams previously determined at $\rho = 0$ and 1 [4,7]. Concentrations of mixture components are specified as a mole fraction (e.g., χ_{DSPC}). We note that the mixtures studied here should be considered pseudo-quaternary because we neglect all components of the aqueous buffer. Most important, we neglect water on the basis that its chemical potential is constant at every lipid composition examined because of the presence of excess water. Even so, the water composition of each phase varies over the phase diagram, and we do not measure its fraction in any of the phases.

Fluorescent dyes can provide a unique signal of their local environment, for example, by a change in wavelength or intensity in different phase environments. Here we make use of changes in FRET as donor and acceptor dyes partition between coexisting phases. When dyes concentrate within the same phase, their average separation distance decreases, resulting in a compositional region of enhanced FRET efficiency (REE). When dyes prefer different phases, the increase in average dye separation distance leads to a region of reduced FRET efficiency (RRE). We used the donor/acceptor FRET dye pair DHE/BoDIPY-PC (which partition into Lo and Ld phase, respectively) to generate RREs when Ld and Lo phases coexist. In a second type of experiment, described below in more detail, we used the FRET pair TOE/BoDIPY-PC (both of which partition strongly into the Ld phase) to generate REEs, but with an additional dye, C12:0-DiI, added to the energy transfer chain. C12:0-DiI also partitions strongly into the Ld phase, and accepts energy selectively from BoDIPY-PC. This "3-dye method" can be especially sensitive, in at least some regions of the phase diagram, to the formation of a small fraction of Ld phase.

2.3. FRET

We used FRET to find many of the phase boundaries in the quaternary phase diagram. All samples for FRET measurement were prepared by use of rapid solvent exchange (RSE) to minimize cholesterol de-mixing [28]. Lipids and dyes were dispensed into glass tubes with a 25 μL Hamilton syringe attached to a repeating dispenser (Hamilton USA, Reno, NV). RSE buffer (0.500 mL, 200 mM KCl, 5 mM PIPES, 1 mM EDTA, pH 7.0) was added to the chloroform solution of lipids and dyes. Samples were vortexed while vacuum pumping for 1 min, sealed under argon and placed in a water bath at 60 °C. Samples were cooled at 2 °C/h to 23 °C and equilibrated at room temperature for 48 h before measurement.

1.90 mL of RSE buffer was added to 0.100 mL of sample to yield 25 μM lipid vesicles in the cuvette. Data were collected on a Hitachi F-7000 FL spectrofluorimeter (Hitachi High Technologies America, Inc., Schaumburg, IL) at an ambient temperature of 23 °C.

Samples contained 250 nmol of the lipid mixture. Dye concentrations were 0.5 mol% for DHE and 0.05 mol% for BoDIPY-PC. Using 2.5 nm bandpass for excitation and emission slits and 10 s integration time, intensity was measured in six channels (ex/em): DHE fluorescence (327/393 nm), BoDIPY-PC sensitized emission (327/517 nm), BoDIPY-PC direct fluorescence (500/517 nm), and light scattering (440/430 nm). For the 3-dye experiment, dye concentrations were 0.7 mol% for TOE, 0.07 mol% for BoDIPY-PC, and 0.05 mol% for C12:0-DiI. Fluorescence was measured in six ex/em channels using 2.5 nm bandpass slits and 10 s integration time: TOE fluorescence (280/340 nm), BoDIPY-PC sensitized emission (280/516 nm), BoDIPY-PC direct fluorescence (509/516 nm), C12:0-DiI sensitized emission (509/575 nm), C12:0-DiI direct fluorescence (549/575 nm), and vesicle light scattering (440/430 nm). Control samples were prepared to correct for non-FRET contributions as described previously [7,28]. Briefly, corrections account for non-FRET contributions of direct fluorescence emission from donor and acceptor, and scattering of excitation light by the vesicle suspension.

2.4. GUV imaging

2.4.1. GUV preparation by electroswelling

GUVs were prepared by the method of "electroswelling" [29,30]. Briefly, each sample contained 250 nmol of a lipid mixture in 200 μL chloroform, with 0.02 mol% C12:0-DiI. A lipid film was created by evenly dispersing the chloroform solution onto indium tin oxide (ITO)-coated microscope slides (Delta Technologies Ltd, Stillwater, MN) on a hotplate set at 55 °C. After the residual solvent was removed under vacuum, ITO slides were sealed with Buna-N O-rings to create a chamber and filled with 100 mM sucrose solution. The films were incubated for 2 h at 55 °C with an AC field of 5 Hz, ±1 Vpp, using a Wavetek FG2C function generator (Meterman, Everett, WA) and Digi-sense temperature controller R/S (Cole Palmer, Vernon Hills, IL) to produce GUVs, followed by a 10 h cooling period. GUVs were harvested into 100 mM glucose solution and allowed to settle for 1 h before microscopy observations at 23 °C.

2.4.2. Fluorescence microscopy

A Nikon Diaphot-TMD microscope (Micro Video Instruments, Inc., Avon, MA) was used for wide-field fluorescence microscopy at 23 °C, using a 60× 1.4 NA oil immersion objective. BoDIPY-PC and C20:0-DiI (at 0.02 mol%) were chosen as a dye pair with different phase partitioning: in DSPC-containing mixtures, BoDIPY-PC partitions into the Ld phase whereas C20:0-DiI prefers DSPC-rich Lo and Lβ phases over disordered phases [4]. GUVs in the Ld + Lo region were imaged with BoDIPY-PC and naphthopyrene dyes at 0.02 and 0.033 mol%, respectively. In this system, naphthopyrene partitions into the Lo phase over the Ld phase. GUVs exhibiting spatially modulated Ld + Lo phase domains were also imaged with complementary BoDIPY-PC and naphthopyrene dyes. For critical point investigation, GUVs were labeled with C12:0-DiI at 0.02 mol%. We used a combination of tactics to minimize light-induced artifacts [5]: low exposure times (100–300 ms); neutral density filters at OD = 1.0; and minimizing sample exposure to light by using dim halogen transmitted light to locate and focus on GUVs [30]. Images were taken with a Photometrics charge-coupled device camera CoolSNAP HQ2 (Tucson, Arizona). C12:0-DiI and C20:0-DiI dyes were imaged with ex/em 540–552 nm/565-605 nm; BoDIPY-PC 460–500 nm/515–560 nm; naphthopyrene 426–446 nm/460–500 nm. Images from GUVs containing multiple dyes were color-merged using NIS software: BoDIPY-PC green, C20:0-DiI and C12:0-DiI red, and naphthopyrene blue. Image contrast was enhanced with NIS Elements Basic Research Software (MVI, Inc.).

2.4.3. Critical point investigation and percolation map

The critical point at ρ = 1 was previously determined by Heberle et al. [7] to be at DSPC/DOPC/chol = 0.26/0.34/0.40. Critical points for ρ = 0.50 and ρ = 0.70 were experimentally determined in this study by determining the continuous (percolating) phase as a function of composition to obtain a percolation map. The region of the Ld + Lo percolation map near the critical point was constructed for ρ = 0.50 and ρ = 0.70, by analyzing on average ~100 GUVs at each composition. The locus of compositions for which connectivity in GUVs changes from Ld to Lo was extrapolated to its intersection with the previously determined Ld + Lo upper phase boundary, thereby marking the critical point at these ρ values.

2.5. Constructing 4-component phase diagrams

The 3-dimensional model of the 4-component phase diagram was developed using Environmental Systems Research Institute's (ESRI) ArcGIS for Desktop Advanced software suite version 10.1 (Redlands, California), a geographic information system designed to view and manipulate spatial data. The primary modeling environment was the 3D visualization application ArcScene. A spherical coordinate system was used to derive a relative frame of reference for each component of the phase diagram. Data were imported into an undefined coordinate system in ArcScene as XYZ point cloud data that were then manually edited into vector geometry, specifically line and polygon feature classes. The resulting 3-dimensional 4-component model is interactive and rotatable, with all phase volumes and the bounding tetrahedron independent of one another including adjustment of chromaticity, illumination, and transparency. Individual 2D phase diagrams, corresponding to faces of tetrahedron and slices at various ρ values, were constructed using Mathematica 7 (Wolfram Research, Champaign, IL).

3. Results

3.1. 2-Dye FRET: DHE → BoDIPY-PC

Trajectories T1 and T2 were used to locate the upper boundary of region 5 between ρ = 0 and 1. (See Fig. 1 legend for a detailed description of trajectories and their endpoints). Within the Ld + Lo coexistence region, the dyes separate from each other and the FRET signal decreases. In favorable cases, depending on the lipid mixture and location of the trajectories in composition space, a change in slope of the FRET signal is significant and easily identified when the phase boundary is crossed. Fig. 1 shows the locations of trajectories T1–T6 (panels A and B) and ρ planes (panel C) within the composition space. Figs. 2 and 3 show 2-dye FRET data for trajectories T1 and T2, respectively, which are used to find phase boundaries at different ρ values. Table S1 summarizes boundary compositions in terms of component mole fractions.

3.2. 3-Dye FRET: TOE → BoDIPY-PC → C12:0-DiI

The 2-dye FRET method mentioned in the previous section was developed to allow for unambiguous determination of phase boundaries by visual inspection [31]. The method exploits the highly nonlinear concentration variation, along a tieline, of dyes that partition strongly between coexisting phases. In many cases, there is an abrupt change in sensitized acceptor emission (SAE) at one or both phase boundaries — this is especially true when SAE shows little variation within the single phase regions. For many years our studies of phase behavior yielded imprecise results for some phase boundaries close to the binary axis of high-melting lipid/chol, primarily due to a steep compositional dependence of SAE for Ld-preferring dyes in single-phase gel and Lo regions. This steep dependence may be due in part to a highly nonideal mixing of these probes in an unfavorable ordered environment. In these cases, the change in slope at the phase

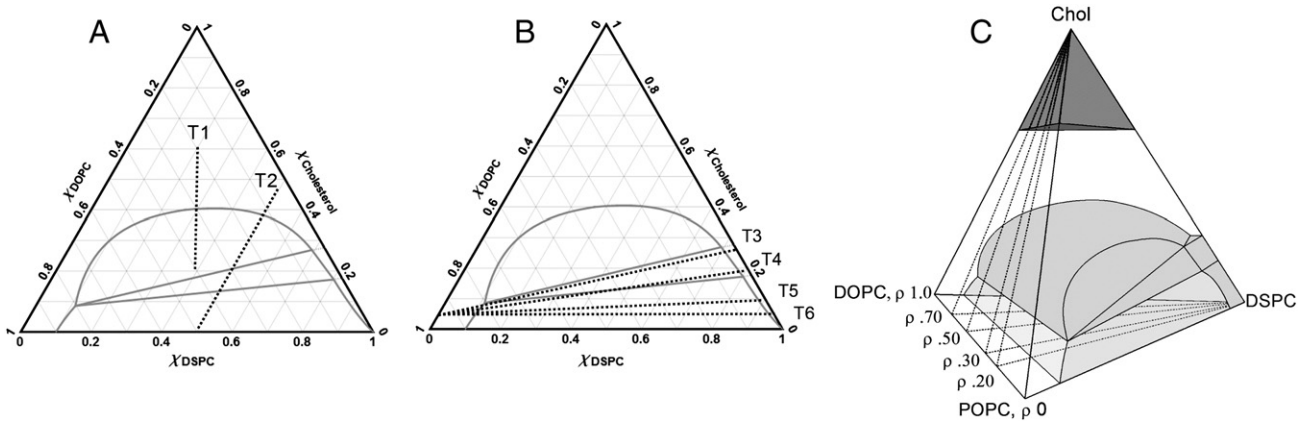

Fig. 1. Compositional trajectories (dashed lines) T1–T6 are located in the 4-component phase diagram. (A) 2-Dye trajectories T1–T2; T1 is along $0.20 \le \chi_{DSPC} \le 0.40$ between cholesterol concentration 0.20 or $0.25 \le \chi_{CHOL} \le 0.50$ or 0.60 at ρ values of 0, 0.30, 0.50, 0.70, and 1.0; T2 is along constant $\chi_{DSPC} = 0.50$ and cholesterol concentration $0 \le \chi_{CHOL} \le 0.45$ at ρ values of 0, 0.30, 0.50, 0.70. For convenience, T1 and T2 are only shown at $\rho = 1.0$ and boundaries for DSPC/DOPC/chol are drawn (solid lines); (B) 3-dye trajectories T3–T6 (dashed lines). T3 is $0 \le \chi_{DSPC} \le 0.732$ and $0.054 \le \chi_{CHOL} \le 0.268$; T4 is $0 \le \chi_{DSPC} \le 0.80$ and $0.054 \le \chi_{CHOL} \le 0.20$; T5 is $0 \le \chi_{DSPC} \le 0.90$ and $0.054 \le \chi_{CHOL} \le 0.10$; T6 is $0 \le \chi_{DSPC} \le 0.95$ and $0.054 \le \chi_{CHOL} \le 0.05$. All trajectories were prepared at ρ values of 0, 0.20 or 0.30, 0.50, 0.70, and 1.0; (C) placement of ρ "slices" within the quaternary phase diagram. All ρ slices share common chol and DSPC endpoints, with varying $\rho = [DOPC] / ([DOPC] + [POPC])$.

boundary is often subtle, and easily obscured by limited compositional resolution and experimental noise.

We have developed a new method that circumvents this problem by the addition of a third dye that (i) partitions strongly into Ld, and (ii) selectively accepts energy from the second dye (i.e., the original FRET acceptor in the 2-dye experiment). The SAE of the second dye is reduced by the presence of the third dye, in direct proportion to the transfer efficiency $E_{2 \to 3}$. Crucially, $E_{2 \to 3}$ is highly nonlinear along a tieline, particularly near the ordered phase boundary, where the probes are concentrated in the Ld phase. By varying the concentration of the third dye, the slope near the Lo boundary can be "tuned" to contrast strongly with the adjacent single phase Lo or gel region. A quantitative model for this behavior is developed in the Appendix, and a description of how a two-dye SAE curve is systematically altered by the addition of the third dye is provided in the Supporting Materials.

We measured sensitized emission of BoDIPY-PC upon selective illumination of TOE, with C12:0-DiI added to quench BoDIPY-PC fluorescence via FRET. A series of different trajectories was prepared, each with 50 samples along with additional appropriate controls, labeled as T3–T6. (See Fig. 1 legend for a description of trajectories and their endpoints). Trajectories were prepared at $\rho = 0$, 0.20 or 0.30, 0.50, 0.70, and 1 (Fig. 1B and C). At a sufficiently high concentration of C12:0-DiI (0.05 mol%), the ordered (Lo or gel) boundary is clearly observed as a drop in BoDIPY-PC fluorescence upon crossing the phase boundary from the single phase (Lo or gel) region.

SAE data shown in Fig. 4 (trajectory T3) and S1–S3 (trajectories T4–T6) were fit to Eq. (A.9). Arrows indicate locations of the boundaries determined by visual inspection. Table S1 summarizes the boundary locations for all trajectories. We find that RHS boundaries shift to lower χ_{DSPC} as DOPC is replaced with POPC: A smooth monotonic shift is apparent for all trajectories T3–T6, consistent with better mixing of DSPC in POPC than in DOPC. Fig. 5 summarizes the phase boundary shift as DOPC is replaced with POPC, revealing the shape of the volume between $\rho = 0$ and 1.

In addition to the thousands of samples covering the entire composition space needed originally to solve the phase diagrams of DSPC/DOPC/chol [4] and DSPC/POPC/chol [7], targeted linear sample trajectories were useful for precisely locating boundaries. The 3-dye method was useful for determining the RHS boundaries. Based on the analysis of these data, we found that relatively small adjustments should be made to our previously published 3-component phase diagrams [4,7].

3.3. Microscopy of GUVs

3.3.1. Phases observed by GUVs

We are especially interested in the transition through the region of modulated phases [23,24] from macroscopic to nanoscopic size scales. Representative GUV images are shown in Fig. 6: (A) macroscopic Ld + Lo coexistence at $\rho = 1$; (B) nanoscopic Ld + Lo coexistence at $\rho = 0$, and (C) modulated morphology at $\rho = 0.2$. Fig. 6D is a representative image for the Ld + Lβ phase region. We have previously found that Ld + Lβ domains are macroscopic at all ρ values [4].

3.3.2. Percolation map and critical points

Critical points for $\rho = 0.50$ and 0.70 were determined as described in Section 2.4.3. GUVs near the critical point exhibited irregular domain boundaries, consistent with proximity to a critical point. Critical points (stars) for $\rho = 0.50$ and 0.70 were found at DSPC/DOPC/POPC/chol = 0.22/0.22/0.22/0.34 and 0.24/0.12/0.27/0.37, respectively (Fig. 7). Locations of critical points are summarized in Table S1. The $\rho = 1$ critical point was previously determined at DSPC/DOPC/chol = 0.26/0.34/0.40 [7]. By extrapolating a line connecting these three experimentally determined points, we estimate the critical point at $\rho = 0$ to be at DSPC/POPC/chol = 0.18/0.54/0.28.

4. Discussion

4.1. Tour of the quaternary phase diagram

Overview of DSPC/DOPC/POPC/chol phase diagram

Fig. 8 shows each individual face of the DSPC/DOPC/POPC/chol phase diagram, and Fig. S4 shows planar sections through the phase diagram at $\rho = 0.20$ (panel A), $\rho = 0.50$ (panel B), and $\rho = 0.70$ (panel C). The quaternary phase diagram for DSPC/DOPC/POPC/chol from three perspectives is shown in Fig. 9, and a stereoscopic 3D image is shown in Fig. S5. We describe below the 7 phase volumes (Fig. 9A) of DSPC/DOPC/POPC/chol, starting with the 4 individual ternary faces of the tetrahedron.

Ternary phase diagrams for DSPC/DOPC/chol and DSPC/POPC/chol were described previously [4,7], but are shown here with some phase boundaries adjusted based on our new data. The ternary faces DSPC/DOPC/POPC (Fig. 8C) and DOPC/POPC/chol (Fig. 8D) show rather simple phase behavior. The boundary between Ld phase and coexisting

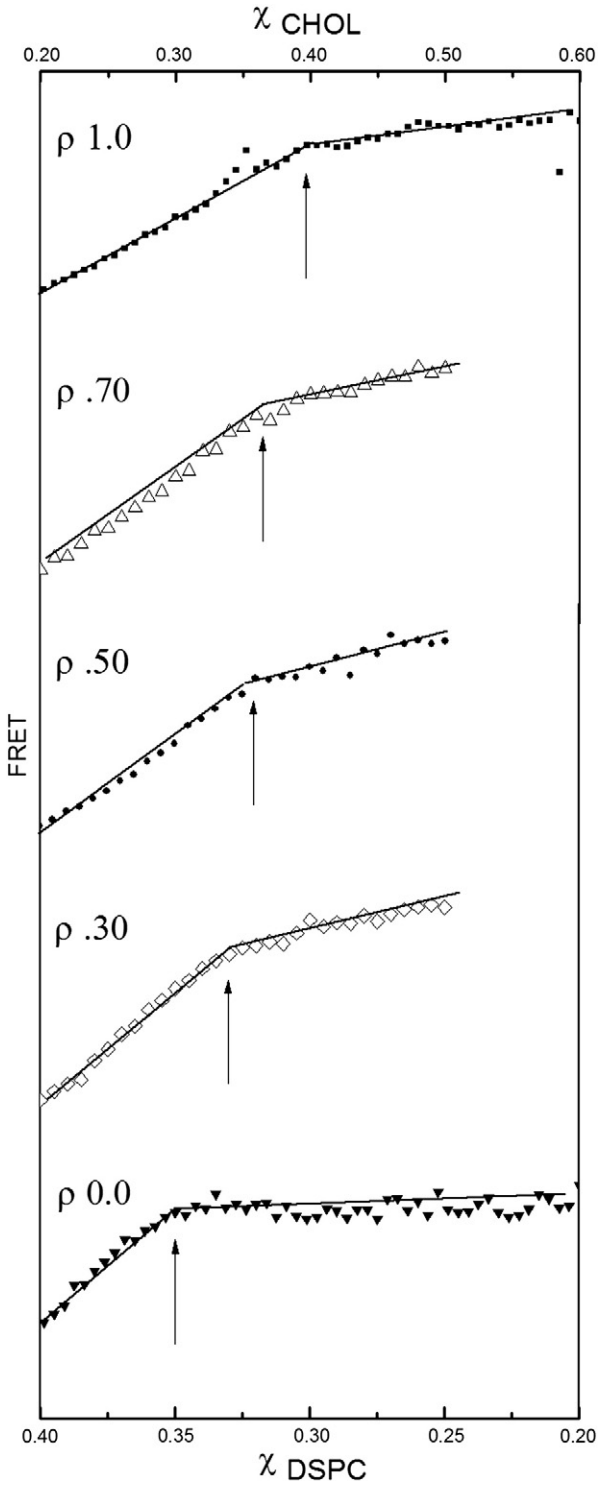

Fig. 2. Upper boundaries of the Ld + Lo region change smoothly from ρ = 0 to 1 along T1. Panels show FRET along T1 using 2-dye pair DHE → BoDIPY-PC to locate boundaries. FRET changes abruptly at the onset of a phase transition, allowing precise boundary determination (solid lines show fit for slope change). Arrows show location of the phase boundary where Ld + Lo phase coexistence appears/disappears.

Ld + Lβ is found at $\chi_{DSPC} = 0.10$ for all ρ values (Fig. 8C). Fig. 8D (the ternary phase diagram for DOPC/POPC/chol) illustrates the uniform transition from Ld to Lo in region 6, along with region 7 for $\chi_{CHOL} > 0.67$.

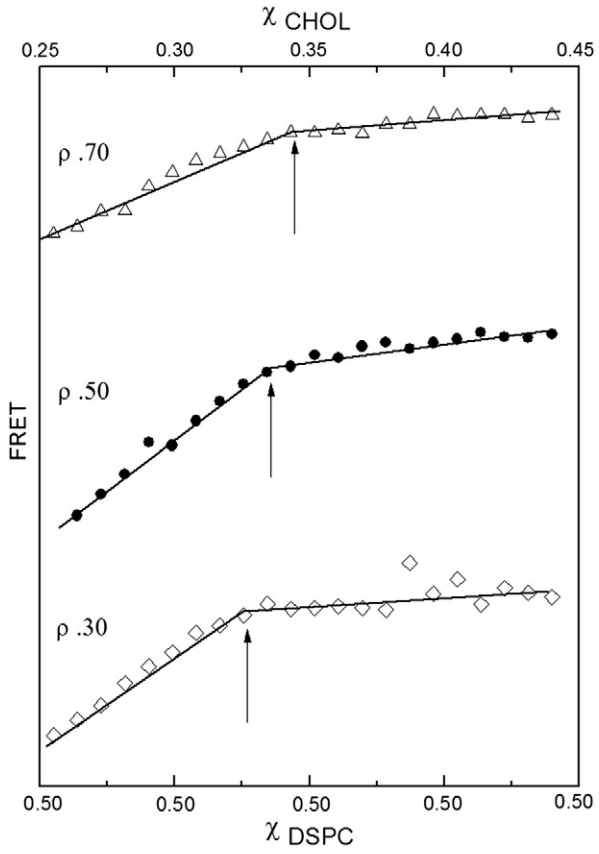

Fig. 3. Upper-RHS boundaries of the Ld + Lo region change smoothly with ρ along T2. Panels show FRET along T2 using DHE → BoDIPY-PC to locate boundaries at ρ = 0.70, 0.50 and 0.30. Arrows show the location of the boundary, which shifts smoothly between ρ = 0 and 1.

4.2. 4-Component regions

4.2.1. Liquid + gel coexistence, Ld + Lβ(β′), region 1

The upper boundary of region 1 is a plane that is also the lower boundary of the 3-phase coexistence region 4. The LHS boundary of Fig. 9A indicates the maximum solubility of DSPC at $\chi_{DSPC} = 0.10$, for both DOPC-rich and POPC-rich Ld phases. This boundary does not change as cholesterol concentration increases. The RHS boundary of region 1 shows that DOPC is rather insoluble in the DSPC-rich Lβ′ phase, with $\chi_{DOPC} < 0.02$ without cholesterol; POPC is more soluble than DOPC in the DSPC-rich solid phase, with $\chi_{POPC} \sim 0.11$ without cholesterol, as previously determined by differential scanning calorimetry [32]. As cholesterol concentration increases, only small changes occur in the RHS boundary, i.e., the solubility of POPC in the gel hardly changes, and the solubility of DOPC only changes from $\chi_{DOPC} < 0.02$ to about 0.03. The maximum solubility of cholesterol in the DSPC-rich Lβ phase is nearly the same at $\chi_{CHOL} = 0.16$–0.18, whether the Lβ phase contains χ_{DOPC} at 0.03 or χ_{POPC} at 0.11. We have found this same maximum solubility of cholesterol of $\chi_{CHOL} \sim 0.17$ for these two Lβ phase mixtures, as well as for Lβ phases of DPPC/DLPC [6], brain sphingomyelin (bSM)/DOPC [8] and bSM/POPC [8].

4.2.2. Gel [Lβ(Lβ′)], region 2

The pure hydrated lipid DSPC at 23 °C is a solid with tilted chains, Lβ′. As found for DPPC, the addition of cholesterol causes the chain tilt to disappear but without the formation of a coexisting phase, i.e., a continuous phase transition occurs in region 2, with Lβ forming from Lβ′ [6]. Region 2 is thus bounded at $\chi_{DOPC} = 0.03$, $\chi_{POPC} = 0.11$, and $\chi_{CHOL} \sim 0.17$.

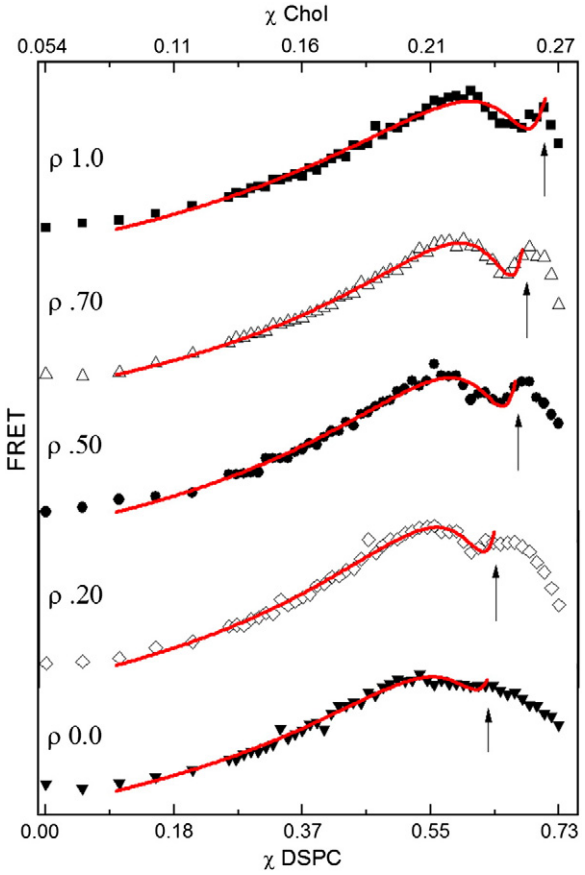

Fig. 4. RHS boundaries along T3 are precisely detected by the use of 3-dye FRET TOE → BoDIPY-PC → C12:0-DiI data along T3 from ρ = 0 to 1. Arrows show the location of the RHS boundary of Ld + Lo coexistence for each ρ value. At low ρ values this boundary is much less sharp. Data for T4–T6 are shown in Figs. S1–S3. Solid lines represent fits to Eq. (A.9), as described in the Appendix and Supporting MATERIALS.

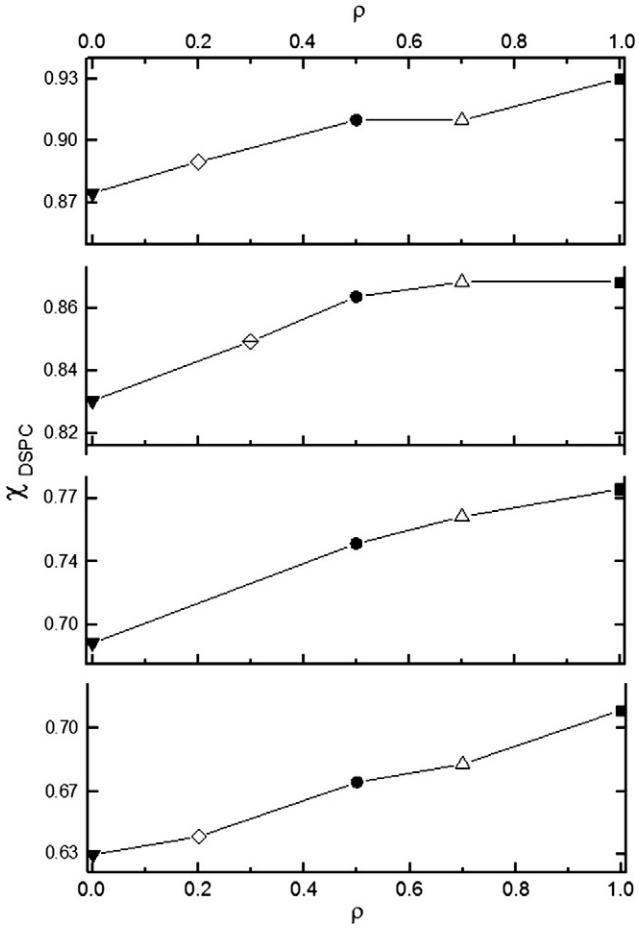

Fig. 5. All RHS phase region boundaries shift smoothly as ρ changes from 0 to 1 along T3–T6. Boundary locations are described by χ_{DSPC}. Filled squares, ρ = 1.0 for T3–T6; open triangles, ρ = 0.70 for T3–T6; filled circles, ρ = 0.50 for T3–T6; diamonds with line, ρ = 0.30 for T4 and T5; open diamonds, ρ = 0.20 for T3 and T6; filled triangles, ρ = 0 for T3–T6.

4.2.3. Liquid-ordered + gel coexistence, Lo + Lβ, region 3

This wedge-shaped region has one edge along the DSPC/chol binary axis from χ_{CHOL} ~ 0.18–0.27. Along this axis, Lβ transitions to Lo with increasing cholesterol fraction, but without evidence of coexisting phases (i.e., a continuous phase change). Away from this binary axis, as low-melting PC increases in the mixture, coexisting phases appear. The upper and lower boundaries of region 3 are not well defined by our data. Instead, these boundaries, which connect to the lower and upper boundaries of region 4, were chosen to be in agreement with Schreinemakers' Rules [33].

4.2.4. 3-Phase coexistence, Ld + Lo + Lβ, region 4

3-Dye data for trajectories T3 and T4 (Figs. 4 and S1, respectively) were used to determine the RHS boundaries of this volume at five ρ values: 0, 0.20, 0.30, 0.50, 0.70, and 1. Remarkably, the upper and lower planes that bound region 4 do not change from POPC-containing mixtures to DOPC-containing mixtures, although the RHS boundaries do change with ρ. For all values of ρ, the Lo phase that separates has χ_{CHOL} ~ 0.25–0.27. The solubility of DSPC in both POPC/chol and DOPC/chol mixtures is the same, and the solubility of chol in the Lβ phase that contains either POPC or DOPC is also nearly the same. Together, these behaviors yield the remarkable observation that the upper and lower boundaries of the three phase region are essentially independent of ρ. These boundary planes are immensely useful because they contain thermodynamic tielines.

4.2.5. Liquid–liquid coexistence, Ld + Lo, region 5

The upper DSPC/DOPC/chol boundary terminates at a maximum χ_{CHOL} ~ 0.40, whereas that of DSPC/POPC/chol terminates at χ_{CHOL} ~ 0.30. A smaller region of immiscibility indicates better mixing of both DSPC and cholesterol with POPC. The upper boundary is established by FRET trajectories (T1 and T2) using the donor/acceptor pair DHE/BoDIPY-PC (Figs. 2 and 3).

The slopes of the bottom tieline in region 5 shows that the chemical potential of cholesterol is ~3-fold greater in the Ld phase than in the Lo phase, consistent with cholesterol interacting more favorably with saturated acyl chains than unsaturated ones. Yet, the Ld phase can accommodate cholesterol up to mole fraction 0.67 without a first-order phase change, instead gradually changing from Ld to Lo as cholesterol fraction increases [6]. In contrast, the Lβ phase can accommodate cholesterol only up to χ_{CHOL} ~ 0.17, above which the cholesterol-rich Lo phase separates in a first-order transition. We note that for plasma membranes having compositions within region 5, as χ_{CHOL} approaches typical values found in cells of ~0.3–0.4 [34], the χ_{CHOL} in each phase becomes similar.

We have previously reported the existence of an intermediate morphology of "modulated phases" within the Ld + Lo region in DSPC/DOPC/POPC/chol [23,24]. Within the Ld + Lo coexistence region, the phase domain size changes from the nanometer scale at ρ = 0 to the micron scale at ρ = 1. This size scale transition is accompanied by a visible morphology transition over a narrow range of compositions as DOPC is replaced with POPC, i.e., phase coexistence exhibits patterns, with one example illustrated by the GUV image in Fig. 6C. In the compositional region near χ_{DSPC} = 0.39–0.45 and χ_{CHOL} = 0.22–0.25, the region of modulated phase domain morphology appears between ρ = 0.15–0.30 [23].

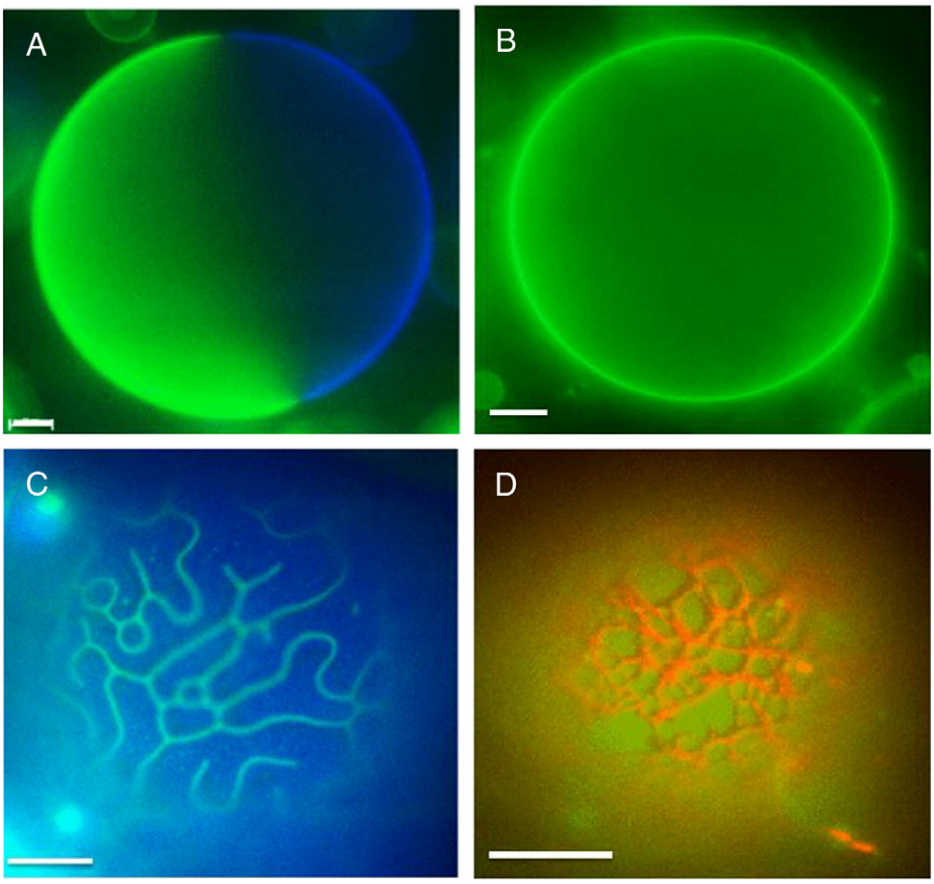

Fig. 6. GUV images identify phase regions at various compositions of DSPC/DOPC/POPC/chol. (A) Macroscopic Ld + Lo coexistence at 0.45/0.30/0/0.25; (B) nanoscopic Ld + Lo coexistence at 0.45/0/0.30/0.25; (C) modulated phase morphology at 0.45/0.06/0.24/0.25; (D) Ld + Lβ phase coexistence at 0.45/0.50/0/0.05. Images are color-merged using Nikon multichannel acquisition: C20:0-DiI (red), BoDIPY-PC (green), and naphthopyrene (blue). Temperature 23 °C. Scale bar 10 μm.

4.2.6. One phase varying continuously from Ld to Lo, region 6

This region is shown as its entire phase volume in Fig. 9A, and the intersection of that volume with the $\chi_{DSPC} = 0$ face of the tetrahedron in Fig. 8D. This is a region of continuous phase change, with no boundary marking a transition between Ld and Lo.

4.2.7. Coexisting cholesterol monohydrate crystals and a cholesterol-saturated Lo phase, region 7

When cholesterol concentration exceeds $\chi_{CHOL} \sim 0.67$, cholesterol precipitates as crystals of the monohydrate. This phase boundary was determined previously [35], and results are shown here for completeness.

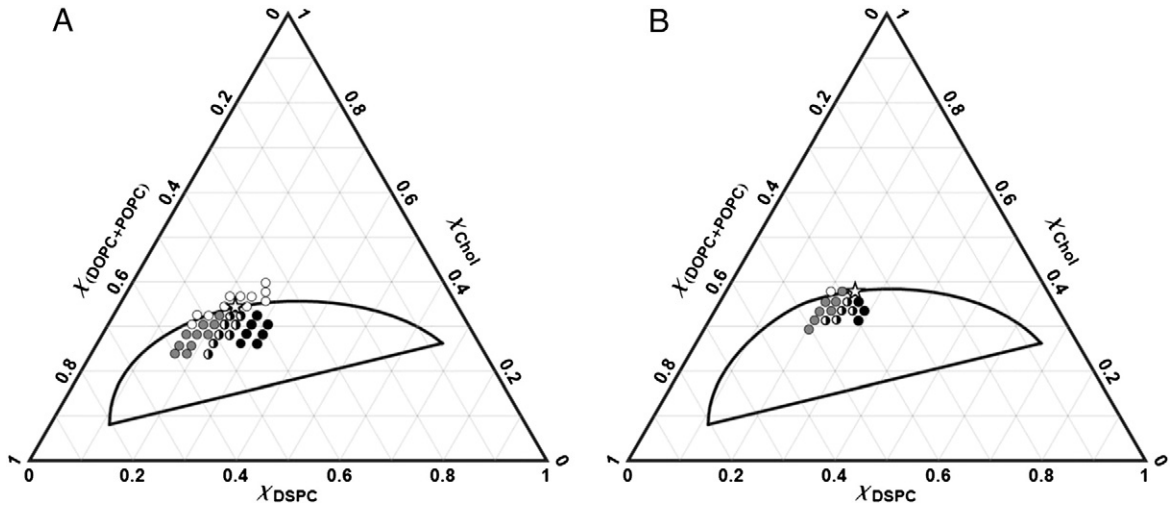

Fig. 7. Percolation maps enable finding critical points, marked by small stars for (A) ρ = 0.50 and (B) ρ = 0.70. Boundaries for the Ld + Lo region are shown for reference. Filled circles, GUVs within Ld + Lo phase coexistence with Lo as the percolating phase; gray circles, Ld is the percolating phase; open circles, GUVs are uniform within a one phase region; half black/white circles, GUVs exhibiting both types of connectivity. Critical points, (A) 0.22/0.22/0.22/0.34; (B) 0.24/0.117/0.273/0.37. Locations of critical points are summarized in Table S1. The ρ = 1.0 critical point has been previously determined at DSPC/DOPC/chol = 0.26/0.34/0.40 [8]. By extrapolating a line connecting these three experimentally determined points, we estimate the critical point at ρ = 0 to be at DSPC/POPC/chol = 0.18/0.54/0.28 (Fig. 9C and Table S1).

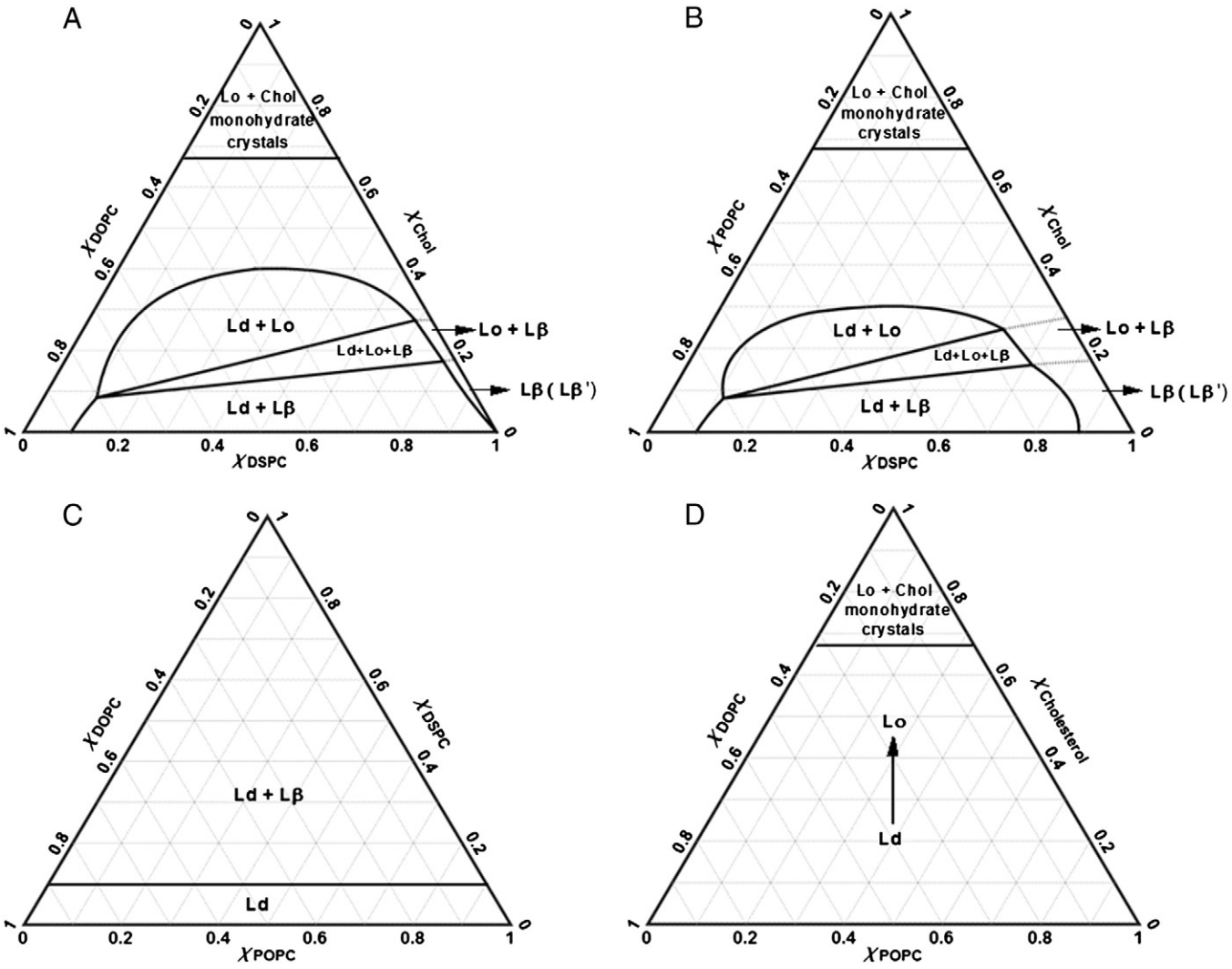

Fig. 8. The four faces of the DSPC/DOPC/POPC/chol tetrahedron are each 3-component phase diagrams. (A) DSPC/DOPC/chol; (B) DSPC/POPC/chol; (C) DSPC/DOPC/POPC; (D) DOPC/POPC/chol. Solid black lines are well-determined by experimental measurement, dashed lines show estimated boundaries.

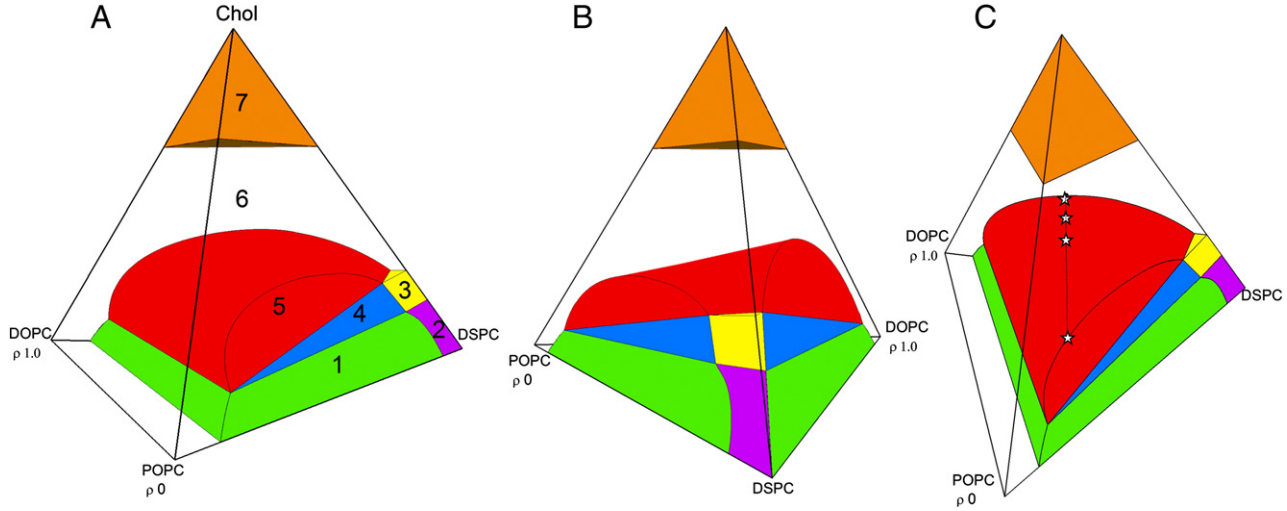

Fig. 9. Tetrahedral phase diagram of DSPC/DOPC/POPC/chol with all phase volumes labeled. (A) region 1 (green), 2-phase Ld + Lβ coexistence; region 2 (purple) 1-phase Lβ (Lβ′); region 3 (yellow) 2-phase Lo + Lβ becomes a continuous phase transition along the binary axis; region 4 (blue) 3-phase Lo + Ld + Lβ; region 5 (red) 2-phase Ld + Lo; region 6 (white) 1-phase varying continuously between Ld and Lo; region 7 (orange) 2-phase crystalline cholesterol monohydrate + cholesterol-saturated Lo phase; (B) clockwise rotation of (A) shows the smooth transition of the upper Ld + Lo boundary from the mixture containing POPC to that containing DOPC. (C) counterclockwise rotation and tilting of (B) shows the line of critical points (stars) along the upper boundary of Ld + Lo. Compositions of the critical points are given in Table S1.

4.3. Some phase transitions might not be first-order

Phase boundaries determined by FRET are based on the principle that dyes partition between coexisting phases, a behavior that is characteristic of first-order phase transitions. In this study, we do not attempt to investigate the nature of the phase transitions, but rather focus on locating the phase boundaries. Clearly, some of the observed transitions cannot be first-order, such as the nano-to-macro domain size transition in region 5 (Ld + Lo). In this regard, it might also be the case that transitions along the DSPC/chol binary axis are not first-order [36], but we do not pursue that issue here.

4.4. Maximum cholesterol solubility in Lβ

We observe that the maximum solubility of cholesterol in the Lβ phase is χ_{CHOL} ~ 0.18 when DOPC constitutes a small fraction (~3 mol%) of the Lβ phase [4,7]. In the Lβ phase that has χ_{POPC} ~ 0.12 the maximum solubility of cholesterol is χ_{CHOL} ~ 0.16. These observations might mean that the POPC-containing Lo phase forms somewhat more readily than the DOPC-containing Lo phase. Or, perhaps cholesterol within the Lβ phase at χ_{POPC} ~ 0.12 has a higher chemical potential than has cholesterol in the Lβ phase at χ_{DOPC} ~ 0.03. We cannot answer this in the present study. As we have noted previously [6], this maximum cholesterol solubility of χ_{CHOL} ~ 0.17 in the Lβ phase corresponds closely to each cholesterol being surrounded by one shell, i.e., ~6 nearest-neighbor PCs. Apparently, more cholesterol than this cannot be accommodated in Lβ. In contrast, Ld phases of either DOPC or POPC are stable up to χ_{CHOL} ~ 0.67, where cholesterol monohydrate crystals precipitate.

4.5. Location of the region of modulated phase domains

One important aspect of this study is to place the observations of "nanodomains" within the framework of equilibrium phase behavior: The compositional volume of Ld + Lo phase coexistence extends from one face of the tetrahedron continuously through the composition space to another face of the tetrahedron. This finding enables us to frame the origin of the nanodomains detected here at low concentration of DOPC as a "phase question": Why should a liquid phase be more stable as small domains, rather than as one round domain having minimum perimeter and thus minimum unfavorable energy from line tension?

Although we do not attempt to answer this question directly here (but see Amazon et al. [37]), the present study provides a firm basis to pose this question in terms of equilibrium thermodynamics, rather than, for example, dynamic gain or loss of compositional regions as membrane turns over, or proximity to a critical point — bilayer behaviors that describe some systems well, but which are not universally applicable to all observations of small phase domains. For example, the 4-component phase diagram can be used to understand whether a region of nanodomains is indeed a 2-phase coexistence region, or instead is a structured 1-phase region. For the mixture DSPC/DOPC/chol, a 3-phase region of Ld + Lβ + Lo exists just above the 2-phase Ld + Lβ region. This 3-phase region was identified by fluorescence microscopy imaging that directly showed the shape and approximate area fractions of coexisting domains, and FRET data that clearly revealed the linearity of two sides of the phase coexistence triangle [4,7]. In our current study of the 4-component mixture DSPC/DOPC/POPC/chol, we found this 3-phase region, directly observable by microscopy for DOPC-rich mixtures, to "seamlessly" with the smaller putative 3-phase region for DSPC/POPC/chol.

DSPC/POPC/chol mixtures with compositions above the 2-phase Ld + Lβ region appear uniform by fluorescence microscopy imaging of GUVs [5]. The possibility has been raised that this region, which we identify as 3-phase, is actually a 1-phase microemulsion [38], or else a 1-phase region of critical fluctuations [27]. If so, then according to the phase boundaries that we report here for the 4-component mixture, a version of the Phase Rule sometimes termed the "Law of Adjoining Phases" [39] would be violated: As a phase boundary is crossed, one and only one phase can appear or disappear. If a 1-phase region were directly above the Ld + Lβ coexistence region in POPC-rich mixtures, that 1-phase region would meet the 3-phase region Ld + Lβ + Lo when the DOPC fraction becomes sufficiently great. At that boundary, the number of phases would change by 2, in violation of the Law of Adjoining Phases. With this reasoning, Ld + Lo nanodomains would seem to be well-described as coexisting phases.

5. Summary

1. All phase regions of the 3-component mixture DSPC/DOPC/chol can be determined unequivocally, with spectroscopic methods and GUV imaging in agreement as to phase boundaries and phase identity. In contrast, the phase diagram of the 3-component mixture DSPC/POPC/chol shows no visible Ld + Lo domains by optical imaging of GUVs. However, as DOPC is replaced by POPC, phase boundaries determined spectroscopically shift smoothly to new values, with no significant change in the nature of the phase behaviors. These observations are consistent with nanodomains of Ld + Lo in POPC-rich mixtures being phase domains.
2. With two appropriate 3-component phase diagrams in hand, constructing the 4-component phase diagram that joins them requires a relatively modest effort that can enable a clear definition of the phase region where "modulated phase behavior" occurs.
3. Some phase boundaries do not show up clearly when examined by conventional fluorescence spectroscopic methods, but can show up distinctly with a new "3-dye method" that makes use of a second FRET acceptor.
4. Precise measurement of phase boundaries confirms some near-stoichiometric cholesterol compositions χ_{CHOL}: ~0.17 is the maximum solubility of cholesterol in the Lβ phase, corresponding to one shell of PC around each cholesterol molecule; ~0.27 is the minimum cholesterol concentration to form the Lo phase; 0.30 is the maximum cholesterol concentration for Ld + Lo coexistence in DSPC/POPC/chol; 0.40 is the maximum cholesterol concentration for Ld + Lo coexistence in DSPC/DOPC/chol; and 0.67 is the maximum solubility of cholesterol in an Lo phase, corresponding to the high energy of having more than 3 cholesterol molecules in contact [40].

Acknowledgements

We thank Erwin London for providing us with TOE. Support was received from research awards from the National Institutes of Health R01 GM077198 and the National Science Foundation MCB 0842839 (to G.W.F.). T.M.K. was supported in part by the National Institutes of Health research award 1-T32-GM08267.

Appendix A. Derivation of 3-dye FRET

The bilayer contains three different fluorescent dyes, with maximum excitation wavelengths A < B < C. We seek an expression for the fluorescence intensity of dye B upon direct excitation of dye A. The derivation follows [41]. We assume an illumination wavelength λ_0 (with frequency υ_0) that selectively excites A. Furthermore, we assume that the emission spectrum of A overlaps with the excitation spectrum of B but not that of C (i.e., A can transfer energy only to B), and that B transfers energy to C. Ignoring dye self-quenching, we use the following kinetic model for the relevant photophysical processes:

$$
\begin{aligned}
&(h\upsilon_0+)A^0 \xrightarrow{kA_e} A^* \xrightarrow{kA_d} A^0(+h\upsilon_1)\\
&A^* + B^0 \xrightarrow{kB_e} B^* + A^0\\
&B^* \xrightarrow{kB_d} B^0(+h\upsilon_2)\\
&B^* + C^0 \xrightarrow{kC_e} C^* + B^0
\end{aligned}
$$

where the superscripts * and 0 indicate excited and ground states; k_{Ae} is the rate constant for direct excitation of A; k_{Be} and k_{Ce} are rate constants for spontaneous energy transfer to acceptor B (from donor A) and acceptor C (from donor B); and k_{Ad} and k_{Bd} are rate constants for de-excitation of A and B by modes other than energy transfer (including fluorescence at frequencies υ_1 and υ_2).

The rate equation for the excited state concentration of A is:

$$\frac{d\chi_{A^*}}{dt} = k_{Ae}\chi_{A^0}[h\upsilon_0] - k_{Ad}\chi_{A^*} - k_{Be}\chi_{A^*}\chi_{B^0}. \tag{A.1}$$

Assuming low illumination intensity, only a small fraction of fluorophores are in the excited state (e.g., $\chi_{A^*} \ll \chi_A$), which enables the substitutions $\chi_A \approx \chi_{A^0}, \chi_B \approx \chi_{B^0}, \chi_C \approx \chi_{C^0}$. The steady-state approximation leads to an equation for the excited state concentration of A:

$$\chi_{A^*} = \frac{\left(k'_{Ae}/k_{Ad}\right)\chi_A}{1 + (k_{Be}/k_{Ad})\chi_B} \tag{A.2}$$

with the additional substitution $k_{Ae}[h\upsilon_0] = k'_{Ae}$. Applying the same approach to B yields the rate equation:

$$\frac{d\chi_{B^*}}{dt} = k_{Be}\chi_B\chi_{A^*} - k_{Bd}\chi_{B^*} - k_{Ce}\chi_{B^*}\chi_C. \tag{A.3}$$

A steady-state approximation combines Eqs. (A.2) and (A.3), which upon rearranging yields an equation for the excited state concentration of B:

$$F_B^{Aex} \propto \chi_{B^*} = \frac{\left(k'_{Ae}/k_{Bd}\right)(k_{Be}/k_{Ad})\chi_A\chi_B}{[1 + (k_{Be}/k_{Ad})\chi_B][1 + (k_{Ce}/k_{Bd})\chi_C]} = \frac{C_0C_1\chi_A\chi_B}{[1 + C_1\chi_B][1 + C_2\chi_C]} \tag{A.4}$$

where we have defined a FRET metric F_B^{Aex} (sensitized B emission) that is proportional to χ_{B^*}. The quenching constants C_1 and C_2 describe energy transfer between dye pairs $A \rightarrow B$ and $B \rightarrow C$, respectively, and can be related to their respective Förster distances [39]:

$$C_i \approx \frac{\varepsilon {R_{0,i}}^2}{A} \tag{A.5}$$

where A is the molecular area of the membrane and $\varepsilon = \pi\Gamma(2/3) \approx 4.2541$.

Eq. (A.4) shows the dependence of dye B sensitized emission on the concentrations of the three dye species. In a phase-separated bilayer, non-uniform partitioning modulates the dye concentrations within each phase in a manner that depends on the relative amounts of the phases present. For a two-phase system with a total dye molar concentration χ_P^0 and a molar partition coefficient K_P, the concentration of dye in each phase is:

$$\chi_P^1 = \frac{\chi_P^0}{1 - S_2 + S_2K_P} \tag{A.6}$$

$$\chi_P^2 = \frac{K_P\chi_P^0}{1 - S_2 + S_2K_P} \tag{A.7}$$

where superscripts refer to the phase (1 or 2), S_2 is the mole fraction of phase 2, and $K_P > 1$ indicates preference for phase 2. The observed fluorescence of dye B is a mole fraction-weighted sum of its fluorescence in each phase:

$$F_B^{Aex} = (1 - S_2)F_{B,1}^{Aex} + S_2F_{B,2}^{Aex}. \tag{A.8}$$

Using the definition $K'_P \equiv 1 - S_2 + S_2K_P$, combining Eqs. (A.4), (A.6)–(A.8) and rearranging yields:

$$F_B^{Aex} = \frac{\alpha\chi_A^0\chi_B^0K'_C}{K'_A}\left(\frac{(1 - S_2)C_1^1}{[K'_B + C_1^1\chi_B^0][K'_C + C_2^1\chi_C^0]} + \frac{S_2C_0^0C_1^2K_AK_B}{[K'_B + C_1^2\chi_B^0K_B][K'_C + C_2^2\chi_C^0K_C]}\right) \tag{A.9}$$

where α is a constant of proportionality that depends on experimental details (instrumentation and sample concentration), and $C_0^0 \equiv C_0^2/C_0^1$.

Appendix B. Supplementary data

Supplementary data to this article can be found online at http://dx.doi.org/10.1016/j.bbamem.2013.05.020.

References

[1] D. Lingwood, K. Simons, Lipid rafts as a membrane-organizing principle, Science 327 (5961) (2010) 46–50.
[2] S.L. Veatch, K. Gawrisch, S.L. Keller, Closed-loop miscibility gap and quantitative tie-lines in ternary membranes containing diphytanoyl PC, Biophys. J. 90 (2006) 4428–4436.
[3] S.L. Veatch, S.L. Keller, Seeing spots: complex phase behavior in simple mixtures, Biochim. Biophys. Acta 1746 (2005) 172–185.
[4] J. Zhao, J. Wu, F.A. Heberle, T.T. Mills, P. Klawitter, G. Huang, G. Costanza, G.W. Feigenson, Phase studies of model biomembranes: complex behavior of DSPC/DOPC/Cholesterol, Biochim. Biophys. Acta 1768 (2007) 2764–2776.
[5] J. Zhao, J. Wu, H. Shao, F. Kong, N. Jain, G. Hunt, G.W. Feigenson, Phase studies of model biomembranes: macroscopic coexistence of Lα + Lβ, with light-induced coexistence of Lα + Lo phases, Biochim. Biophys. Acta 1768 (2007) 2777–2788.
[6] G.W. Feigenson, J.T. Buboltz, Ternary phase diagram of dipalmitoyl-PC/dilauroyl-PC/cholesterol: nanoscopic domain formation driven by cholesterol, Biophys. J. 80 (2001) 2775–2788.
[7] F.A. Heberle, J. Wu, S.L. Goh, R.S. Petruzielo, G.W. Feigenson, Comparison of three ternary lipid bilayer mixtures: FRET and ESR reveal nanodomains, Biophys. J. 99 (2010) 3309–3318.
[8] R.S. Petruzielo, F.A. Heberle, P. Drazba, J. Katsaras, G.W. Feigenson, Phase behavior and domain size in sphingomyelin-containing lipid bilayers, Biochim. Biophys. Acta 1828 (2013) 1302–1313.
[9] F.A. Heberle, R.S. Petruzielo, J. Pan, P. Drazba, N. Kučerka, R.F. Standaert, G.W. Feigenson, J. Katsaras, Bilayer thickness mismatch controls domain size in model membranes, J. Am. Chem. Soc. 135 (18) (2013) 6853–6859.
[10] A. Pokorny, L.E. Yandek, A.L. Elegbede, A. Hinderliter, P.F. Almeida, Temperature and composition dependence of the interaction of D-lysin with ternary mixtures of sphingomyelin/cholesterol/POPC, Biophys. J. 91 (2006) 2184–2197.
[11] R.F.M. de Almeida, A. Fedorov, M. Prieto, Sphingomyelin/phosphatidylcholine/cholesterol phase diagram: boundaries and composition of lipid rafts, Biophys. J. 85 (2003) 2406–2416.
[12] J.R. Silvius, Fluorescence energy transfer reveals microdomain formation at physiological temperatures in lipid mixtures modeling the outer leaflet of the plasma membrane, Biophys. J. 85 (2003) 1034–1045.
[13] J.F. Hancock, Lipid rafts: contentious only from simplistic standpoints, Nat. Rev. Mol. Cell Biol. 7 (2006) 456–462.
[14] P.F.F. Almeida, A. Pokorny, A. Hinderliter, Thermodynamics of membrane domains, Biochim. Biophys. Acta 1720 (2005) 1–13.
[15] E.L. Elson, E. Fried, J.E. Dolbrow, G.M. Genin, Phase separation in biological membranes: integration of theory and experiment, Annu. Rev. Biophys. 39 (2010) 207–226.
[16] N. Vyas, D. Goswami, A. Manonmani, P. Sharma, H.A. Ranganath, K. VijayRaghavan, L.S. Shashidhara, R. Sowdhamini, S. Mayor, Nanoscale organization of hedgehog is essential for long-range signaling, Cell 133 (2008) 1214–1227.
[17] D. Meder, M.J. Moreno, P. Verkade, W.L. Vaz, K. Simons, Phase coexistence and connectivity in the apical membrane of polarized epithelial cells, PNAS 103 (2006) 329–334.
[18] M. Ge, A. Gidwani, H.A. Brown, D. Holowka, B. Baird, J.H. Freed, Ordered and disordered phases coexist in plasma membrane vesicles of RBL-2H3 Mast Cells. An ESR study, Biophys. J. 85 (2003) 1278–1288.
[19] C. Eggeling, C. Ringemann, R. Medda, G. Schwarzmann, K. Sandhoff, S. Polyakova, V.N. Belov, B. Hein, C. von Middendorf, A. Schönle, S.W. Hell, Direct observation of the nanoscale dynamics of membrane lipids in a living cell, Nature 457 (2009) 1159–1162.
[20] S.J. Sahl, M. Leutenegger, M. Hilbert, S.W. Hell, C. Eggeling, Fast molecular tracking maps nanoscale dynamics of plasma membrane lipids, PNAS 107 (15) (2010) 6829–6834.
[21] T.S. van Zanten, J. Gómez, C. Manzo, A. Cambi, J. Buceta, R. Reigada, M.F. Garcia-Parajo, Direct mapping of nanoscale compositional connectivity on intact cell membranes, PNAS 107 (35) (2010) 15437–15442.
[22] F.A. Heberle, G.W. Feigenson, Phase separation in lipid membranes, Cold Spring Harbor Perspect. Biol. (2011), http://dx.doi.org/10.1101/cshperspect.a004630.
[23] T.M. Konyakhina, S.L. Goh, J. Amazon, F.A. Heberle, J. Wu, G.W. Feigenson, Control of a nanoscopic-to-macroscopic transition: modulated phases in 4-component DSPC/DOPC/POPC/chol giant unilamellar vesicles, Biophys. J. Lett. 101 (2) (2011) L8–L10.

[24] S.L. Goh, J. Amazon, G.W. Feigenson, Towards a better raft model: Modulated phases in the 4-component bilayer, DSPC/DOPC/POPC/CHOL, Biophys. J. 104 (2013) 853–862.
[25] C. Esposito, A. Tian, S. Melamed, C. Johnson, S.Y. Tee, T. Baumgart, Flicker spectroscopy of thermal bilayer domain boundary fluctuations, Biophys. J. 93 (2007) 3169–3181.
[26] S.L. Veatch, P. Cicuta, P. Sengupta, A. Honerkamp-Smith, D. Holowka, B. Baird, Critical fluctuations in plasma membrane vesicles, ACS Chem. Biol. 3 (2008) 287–293.
[27] A.R. Honerkamp-Smith, S.L. Veatch, S.L. Keller, An introduction to critical points for biophysicists; observations in lipid membranes, Biochim. Biophys. Acta 1788 (1) (2009) 53–63.
[28] J.T. Buboltz, G.W. Feigenson, A novel strategy for the preparation of liposomes: rapid solvent exchange, Biochim. Biophys. Acta 1417 (1999) 232–245.
[29] M.I. Angelova, S. Soleau, P. Meleard, J.F. Faucon, P. Bothorel, Preparation of giant vesicles by external AC electric fields. Kinetics and applications, Progr Colloid Polym. Sci. 89 (1992) 127–131.
[30] N.F. Morales-Penningston, J. Wu, E.R. Farkas, S.L. Goh, T.M. Konyakhina, J.Y. Zheng, W.W. Webb, G.W. Feigenson, GUV preparation and imaging: minimizing artifacts, Biochim. Biophys. Acta 1798 (7) (2010) 1324–1332.
[31] J.T. Buboltz, Steady-state probe-partitioning fluorescence resonance energy transfer: a simple and robust tool for the study of membrane phase behavior, Phys. Rev. E 76 (2007) 021903.
[32] P. Ceppi, S. Colombo, M. Francolini, F. Raimondo, N. Borgese, M. Masserini, Two tail-anchored protein variants, differing in transmembrane domain length and intracellular sorting, interact differently with lipids, PNAS 102 (45) (2005) 16269–16274.
[33] J.S. Marsh, Principles of Phase Diagrams, McGraw-Hill, New York, 1935. 122–170.
[34] The AOCS Lipid Library, http://lipidlibrary.aocs.org/, the joint Editors-in-Chief J. L. Harwood, R. J. Weselake, technical Editor W. W. Christie. Last updated 12/21/2012.
[35] J. Huang, J.T. Buboltz, G.W. Feigenson, Maximum solubility of cholesterol in phosphatidylcholine and phosphatidylethanolamine bilayers, Biochim. Biophys. Acta 1417 (1999) 89–100.
[36] T.T. Mills, J. Huang, G.W. Feigenson, J.F. Nagle, Effects of cholesterol and unsaturated DOPC lipid on chain packing of saturated gel-phase DPPC bilayers, Gen. Physiol. Biophys. 28 (2) (2009) 126–139.
[37] J.J. Amazon, S.L. Goh, G.W. Feigenson, Competition between line tension and curvature stabilizes modulated phase patterns on the surface of giant unilamellar vesicles: a simulation study, Phys. Rev. E 87 (2013) 022708.
[38] M. Schick, Membrane heterogeneity: manifestation of a curvature-induced microemulsion, Phys. Rev. E 85 (2012) 031902.
[39] L.S. Palatnik, A.I. Landau, Phase Equilibria in Multicomponent Systems, in: J. Jaffe (Ed.), Holt, Rinehart & Winston, New York, 1964.
[40] J. Huang, G.W. Feigenson, A microscopic interaction model of maximum solubility of cholesterol in lipid bilayers, Biophys. J. 76 (4) (1999) 2142–2157.
[41] J.T. Buboltz, C. Bwalya, S. Reyes, D. Kamburov, Stern–Volmer modeling of steady-state Förster energy transfer between dilute, freely diffusing membrane-bound fluorophores, J. Chem. Phys. 127 (2007) 215101.